1.4 ANALYTICAL TEM CHARACTERIZATION OF MODIFIED F82H and 14YW UNDER SIMULTANEOUS HELIUM AND NEUTRON IRRADIATION COMPARED TO ONLY NEUTRONS AT 500°C

- H.J. Jung, D. J. Edwards, B. Yao, R. J. Kurtz (Pacific Northwest National Laboratory), G. R. Odette, T. Yamamoto, Y. Wu (University of California Santa Barbara)

OBJECTIVE

To characterize the microstructure and chemical evolution of a reduced activation ferritic/martensitic (RAFM) steel and an oxide dispersion strengthened (ODS) alloy irradiated to 21.2 dpa at 500°C and simultaneously injected with 1230 appm of He via an *in situ* He injection (ISHI) technique.

SUMMARY

An RAFM steel and an ODS ferritic alloy (F82H.mod3+CW and 14YW, respectively) were irradiated as part of the HFIR-JP27 irradiation experiment conducted in the High Flux Isotope Reactor to explore He effects in structural alloys. The *in situ* He injection (ISHI) technique is used to implant He up to 9 µm below the surface of a NiAl coated sample at He/dpa levels up to ~50. This report summarizes the current status of TEM characterization of the two irradiated alloys. The He-implanted side of the RAFM alloy exhibited significant swelling due to bubble and void formation - within the matrix, on pre-existing dislocations, and at interfaces within the material. The 14YW alloy exhibited significant swelling even in the absence of implanted He, primarily through large voids that formed on the ODS particles. In addition, significant radiation-induced segregation of the Cr was observed around oxide particles and on lath boundaries, and visible α′ particles could be detected via elemental mapping of the matrix of the 14YW alloy.

PROGRESS AND STATUS

Introduction

Reduced activation ferritic/martensitic (RAFM) steels and oxide-dispersed strengthened (ODS) alloys are being evaluated as structural materials with high swelling-resistance for first-wall materials for future fusion reactors [1,2]. The materials used in the first wall will inevitably endure a harsh thermal and neutron-irradiation environment, an environment made even more difficult by the presence of high levels of He production (10 appm He per dpa) from transmutation [3]. The high levels of He impacts the mechanical properties of ferritic-based alloys through He embrittlement and the formation of He bubbles and voids in the matrix, at lath boundaries, grain boundaries, and at particle-matrix interfaces [4], which can lower the high-temperature tensile and creep properties. A further consequence of the He accumulation is that the bubbles can grow large enough to eventually transition to unstably growing voids, thereby leading to significant swelling [5]. In order to mitigate the rate at which He bubbles transition to voids, alloy microstructures are being designed to provide a high density of nanoscale trapping sites that keep He gas atoms broadly dispersed [1]. Research efforts are currently investigating the effectiveness of different oxide dispersions, as well as understanding the mechanisms of He transport, trapping, and interaction with various defects and interfaces present in irradiated ferritic based alloys.

Due to practical difficulties of assessing material performance in a neutron irradiation environment under conditions relevant to a fusion reactor, a novel approach, the *in-situ* He injection (IHSI) technique, has been used to investigate the effects of simultaneous neutron irradiation and He injection on microstructural evolution of candidate materials, as described in detail [7]. Here we present analytical transmission electron microscopy (TEM) characterization on neutron irradiated and He-injected samples of a modified F82H (RAFM steel) and 14YW (ODS alloy) with a 4 µm thick NiAl layer bonded to one surface. When irradiated with neutrons, the ^{59}Ni isotope undergoes a ^{59}Ni(n, α) reaction and injects some fraction of the energetic He into the ferritic alloy. The samples were irradiated to a dose of 21.2 dpa at 500°C in the JP-27 experiment in the HFIR reactor, which injected an estimated 1230 appm of He into the sample over a uniform depth of 9 µm. Cross-sectional TEM samples were prepared by FIB to

characterize microstructure related features such as He bubbles/voids, dislocation loops/line dislocation, and oxide or carbide particles.

Experimental Procedure

The compositions of the RAFM steel and ODS alloy characterized in this effort are listed in Table 1. Sample F82H-mod.3+CW was modified to reduce the N and Ti levels to 14 ppm and 0.001%, respectively, and add 0.1% Ta. It was austenitized at 1040°C for 30 min, normalized (air-cooled), and tempered at 740°C for 1.5 h. Before the irradiation, 20% cold work was applied to the modified F82H specimen to generate a high dislocation density. 14YW is ODS alloy fabricated through powder metallurgical procedures, described in Ref. 7. All samples were neutron irradiated to a dose of 21.2 dpa at 500°C in the High Flux Isotope Reactor at Oakridge National Laboratory. The thickness of NiAl is 4.7 µm, which gives a He concentration of about 1230 appm in the ferritic matrix extending to a depth of ~9 µm away below the NiAl coating.

Table 1. Composition of examined RAFM/ODS alloys

Alloy	Composition (wt.%) with Fe balance										
	Cr	Ti	$Y(Y_2O_3)$	C	Al	Ta	W	Mn	Si	Ni	V
F82H-mod.3+CW	8.16	<0.005	-	0.097	-	0.1	1.98	0.13	0.10	0.01	0.20
14YW	14.00	-	0.25	-	-	~	3.00	-	-	-	-

Cross-sectional TEM samples, prepared by a FIB (FEI Quanta 3D), were finalized with low-energy surface cleaning (2 keV Ga^+ ion) at ±2° tilt angles. Further surface cleaning to remove FIB artifacts was conducted using low-energy Ar^+ ion beam by a Fischione Model 1040 NanoMill, detailed in Table 2.

Table 2. Nanomilling cleaning condition

High tension (eV)	Beam current (nA)	Time (min)	Milling size (µm)	Tilt angle (°)	Temperature (°C)
900	165	20 (each side)	40 × 20	± 10	-165

The analytical TEM characterization was performed using a newly installed Cs-corrected JEOL ARM 200CF microscope equipped with various detectors, including a Centurio silicon drift detector (SDD) for energy dispersive X-ray spectroscopy (EDS), a Gatan Dual EELS (electron energy loss spectroscopy) system, and HAADF (high angle annular dark field) and BF (bright field) STEM detectors. This instrument can achieve spherically aberration-corrected sub-nanometer and sub-Å probes with high beam currents because of the cold field emission gun (CFEG), allowing enhanced spatial resolution EDS mapping. TEM sample thickness was determined through convergent-beam electron diffraction (CBED). Bright-field TEM images of He bubbles and voids were acquired at an over/under-focus, and this measured value is about 87% of the actual bubble size at a under-defocus of 750 nm [8]. The dislocation loops and line dislocations were imaged using multiple diffraction vectors at two-beam conditions based on both crystallographic projections [9].

Results and Discussion

A surprising observation was the presence of small 1-2 nm cavities at a density of ~10^{22} per m^3 that were distributed in the matrix of F82H-mod.3+CW that experienced only neutron irradiation (Figure 1-a). With no He injection on this side, it is likely that relatively small levels of He, up to 10-15 appm, were formed from the ^{54}Fe (n,α) reaction in the alloy and transmutation of potential B impurities, the latter of which creates He from the ^{10}B isotope [10]. In the absence of a high density of trapping sites, this alloy nucleated visible bubbles with only a relatively small amount of He. Assuming that about 10 appm He is generated from ^{54}Fe and B impurities and all of this He is contained in the visible bubble population, then the estimated He to vacancy ratio is ~0.44, which is about the level expected for bubbles at equilibrium pressure.

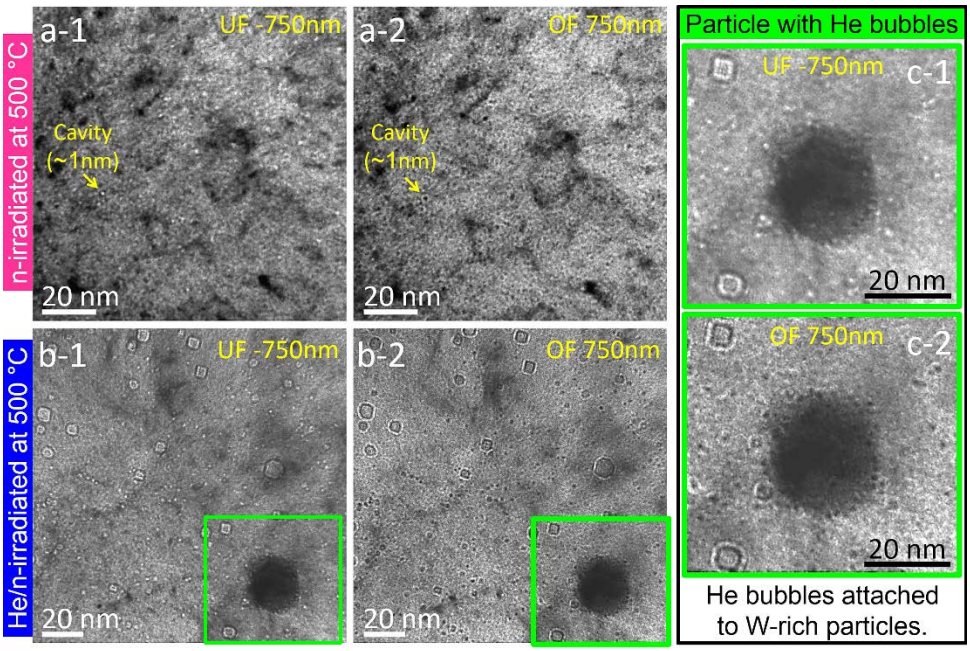

Figure 1. Cavities and He bubbles are visible in F82H-mod.3+CW based on BFTEM images taken at 750 nm of under/over-focus from (a) the side with no He-injection and (b) the side with in-situ He injection. The images in (c) show He bubbles (1~2 nm) and voids (>2nm) forms at W-rich particle/matrix interface. Note that small cavities of 1~2 nm are observed in neutron-irradiated side.

Another transmutation reaction worth noting concerns the W. Substantial Os peaks and lower than expected levels of W were observed in the EDS spectra from both the SEM and TEM analysis of the irradiated samples, and a search of the literature revealed that W converts to roughly 30% Os by 25 dpa in HFIR [11]. This loss of W has been reported by other researchers looking into the effect of W transmutation on the first wall W armor and irradiation hardening of W by Os [12,13]. This reaction occurred equally in both of the samples examined in this study.

As expected, He bubbles ranging in size from 1-3 nm with a density of ~10^{23} per m^3 and larger voids (3~15 nm) are observed in the He-injected side of the neutron irradiated F82H.mod3 alloy (Figure 1-b) as shown using bright-field TEM at an under/over-defocus of ±750nm. A more complete analysis of the cavity distribution is ongoing, but the initial results are summarized in Table 3. A magnified view (Figure 1-c) of the round particle (green box in Figure 1-b), identified as a W-V carbide using EDS mapping, shows He bubbles and voids have nucleated at the interface of the particle. The Cr-rich carbides were found to contain significant levels of W (~12 wt%), and Os (~5 wt%), and lower amounts of V (~1.5 wt%). In our previous work, a high density of small He bubbles less than 2 nm are consistently located at the lath boundaries in conjunction with a large fraction of voids dispersed over the matrix [14]. Furthermore, it has been reported that F82H-mod.3 with cold work exhibits a smaller number of large voids and larger number of small He bubbles than that without cold work when irradiated to 380 appm He / 9 dpa at 500°C [15].

Table 3. Statistics of Cavities in the Two Alloys

Alloy	Non-Implanted Side		He-implanted Side	
	Density (x 10^{23} m^{-3})	Mean Size (nm)	Density (x 10^{23} m^{-3})	Mean Size (nm)
F82H-mod	0.21	1.3	1.1	2.7
14YW	0.06	11.6	1.1	3.1

The non-injected side of the 14YW sample contained relatively large cavities (5 to 30 nm diameter) attached to faceted Y-rich oxide particles (see Figure 2-a), suggesting that the small levels of He produced from the ^{54}Fe reaction accumulated preferentially at the particle/matrix interface and eventually transitioned to large cavities. The He-injected side of the neutron-irradiated 14YW exhibited not only the same association between voids and large Y-rich oxide particles, but a much higher density of small He bubbles (1-3 nm) and large voids (3~30 nm) in matrix as shown in Figure 2-b and Figure 3. Interestingly, several examples were found of He bubbles and voids aligned to <100> directions in the matrix when imaged near an 001 zone axis, indicated as yellow dotted lines in Figure 3. Different from the faceted Y-rich particles, elongated Cr-rich carbide particles nucleated He bubbles and large voids both inside the particle and at the particle/matrix interface. Whether the voids (or cavities) within the elongated particles contain He or not still remains in question and attempts will be made to verify this using EELS. The formation of voids in 14YW shows that coarse scale oxides are not as effective as the nano-oxides in true nano-structured ferritic alloys (NFA) like 14YWT and MA957. Indeed the presence of large voids in 14YW suggests that there may be good and bad oxide microstructures.

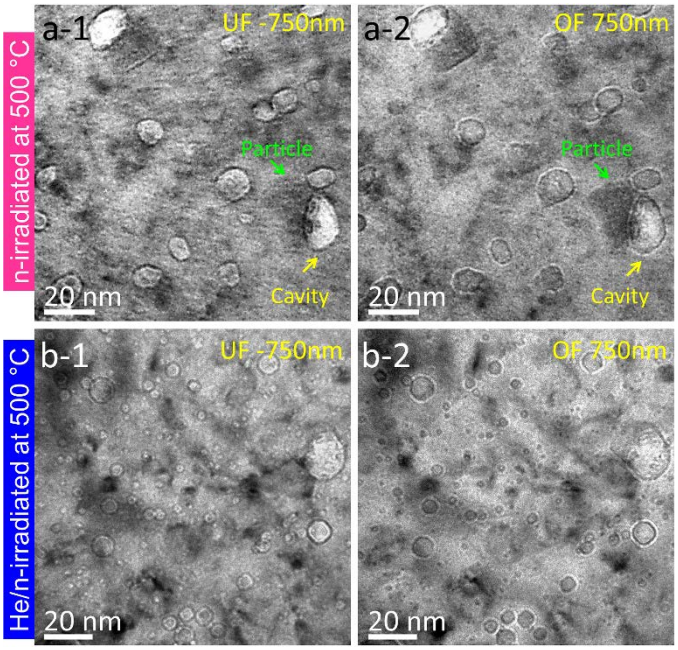

Figure 2. Cavities and He bubbles of 14YW on two sets of BFTEM images at under/over-focus from (a) non-injected side and (b) the in-situ injected side. Note that large cavities ranging from 5 to 30 nm in size are associated with each Y-rich oxide particles.

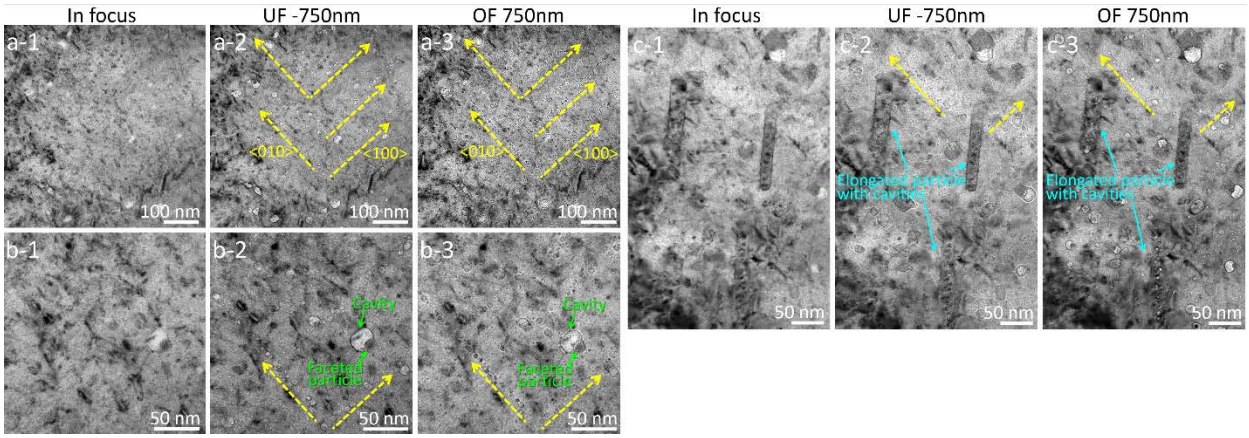

Figure 3. Three sets of through-focus BFTEM images taken near an [001] zone axis in in the He-injected side of alloy 14YW show (a) He bubbles and cavities aligned to <100> directions (along yellow arrow), (b) large cavities (green) attached to rounded rectangular particle surface, and (c) large cavity and He bubbles (light blue) formed at elongated particles inside (c). Note that there are two different particles, one is a round Y-rich oxide phase and the other are elongated Cr-rich carbides.

In order to identify the particle composition and explore chemical evolution during irradiation, EDS elemental mapping was conducted, the results of which are presented in Figs. 4 through 8. Figure 4-a presents an overview of particle distribution predominantly located at lath boundaries in the non-injected side of F82H-mod.3+CW based on bright-field/dark-field TEM images. Figure 4-b shows bright field (BF)/HAADF STEM images with corresponding elemental EDS mapping. There are two types of particles revealed in the maps: a very low density of small W-C carbides (rounded shape) and large Cr-rich carbide particles (elongated shape). Figure 5 provides a comparable set of images and elemental maps from the He-injected side of the neutron irradiated F82H-mod.3+CW, demonstrating the same evidence of chromium carbides and spherical W-V carbides as observed in Figure 1-c.

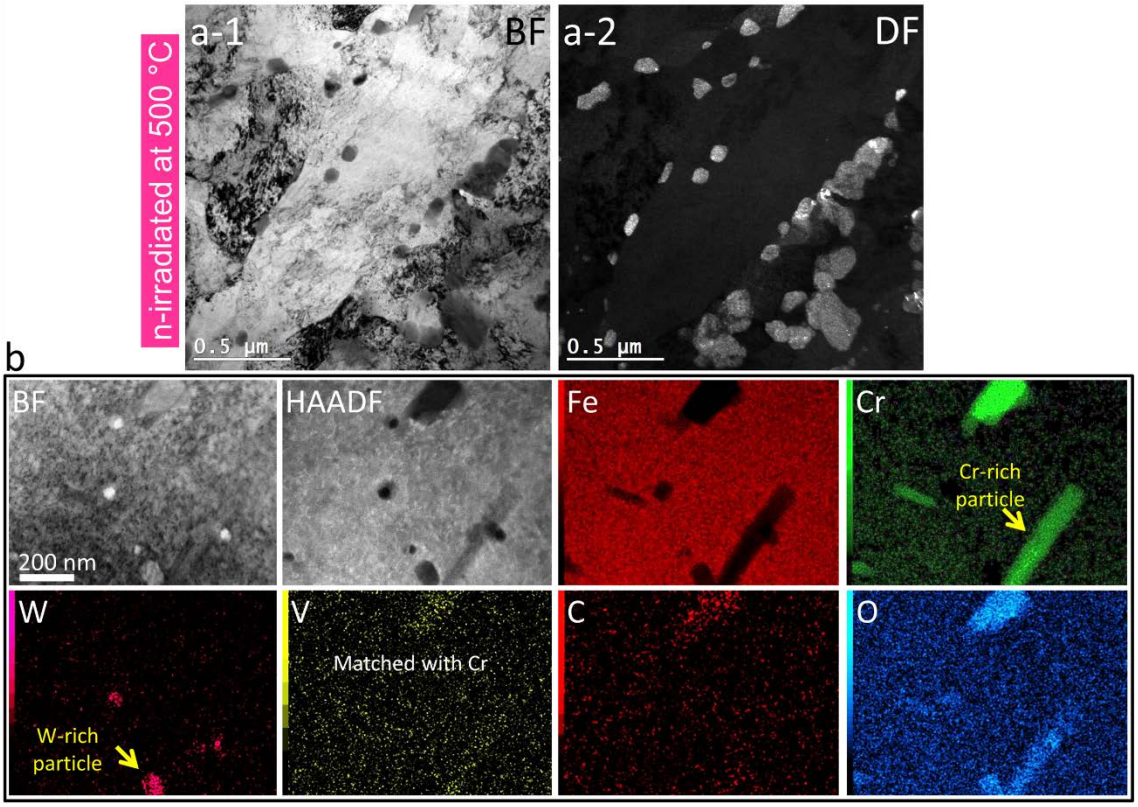

Figure 4. (a) BF and DF TEM images showing Cr-rich carbide particles formed predominately on the lath boundaries in the neutron-irradiated F82H-mod.3+CW. BF and HAADF STEM images with elemental EDS mapping are provided in (b). Note that there are W-rich oxide particles and Cr-rich particles, with the Cr-rich particles generally much larger than the W-rich particles. Vanadium is segregated in Cr-rich particles.

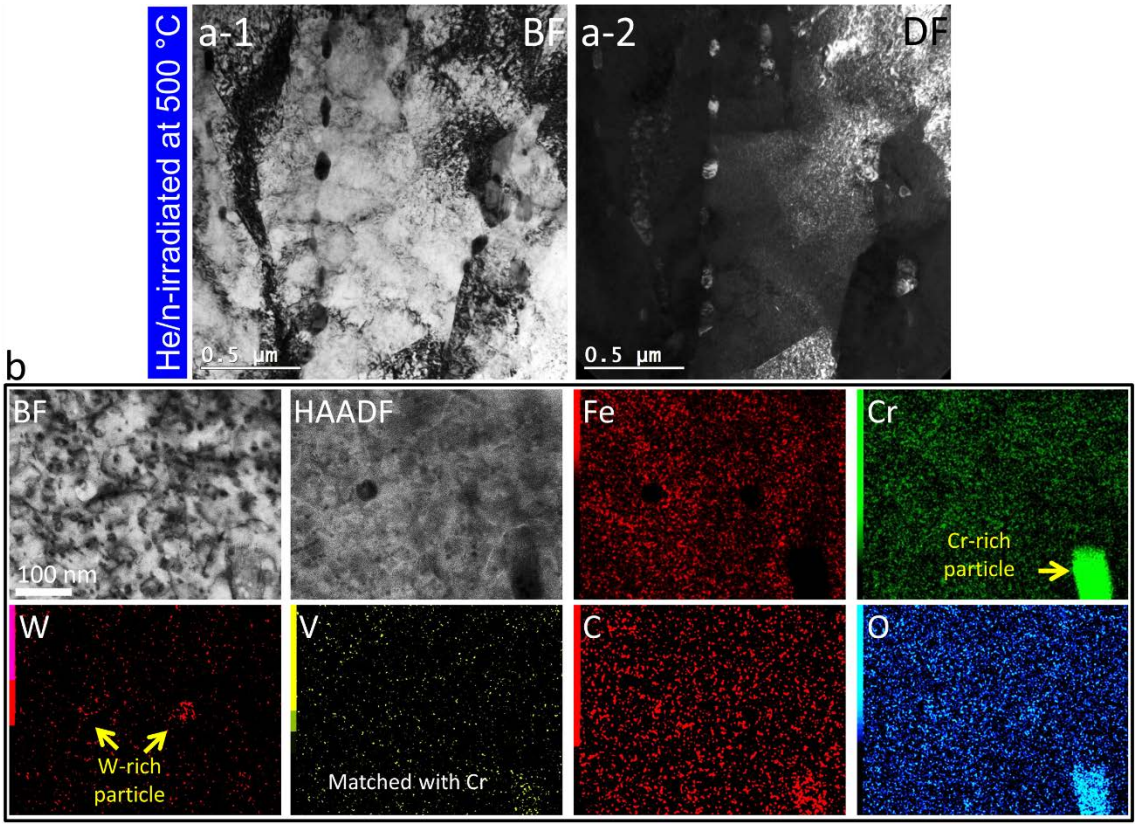

Figure 5. (a) BF and DF TEM images showing particles formed predominately at lath boundaries in the He injected side of F82H-mod.3+CW. (b) BF and HAADF STEM images with elemental EDS mapping reveal the phases in this alloy. Note that there are small W-rich particles and Cr-rich carbides, but no evidence of α′ formation in this alloy.

Figure 6-a displays BFTEM images showing particles from neutron-irradiated 14YW. BF and HAADF STEM images at low and high magnification (6-b and 6-c respectively) with elemental EDS mapping of the indicated elements. There are 3 types of particles identified from EDS mapping. The first are large Cr-rich carbides of 50-500 nm located predominately at grain boundaries. The other two are small spherical W-rich oxide particles of 10-50 nm and small Y-rich oxide particles of 10-50nm, both of which are located in the grain interior. The Y-rich oxide particles are present in a much more uniform distribution and higher number density than the W-rich oxide particles, and contain significant Si, suggesting the oxide particles are actually a Y-Si-O phase. Vanadium, formed due to transmutation, is agglomerated in Cr-rich particles. Phase separation of Cr-rich α' (bcc) at high magnification (Cr map in Figure 6-c) is verified in the elemental maps, as well as segregation to lath boundaries and around oxide particles. In contrast, no α' formation was detected using elemental mapping in the F82H-mod.3+CW.

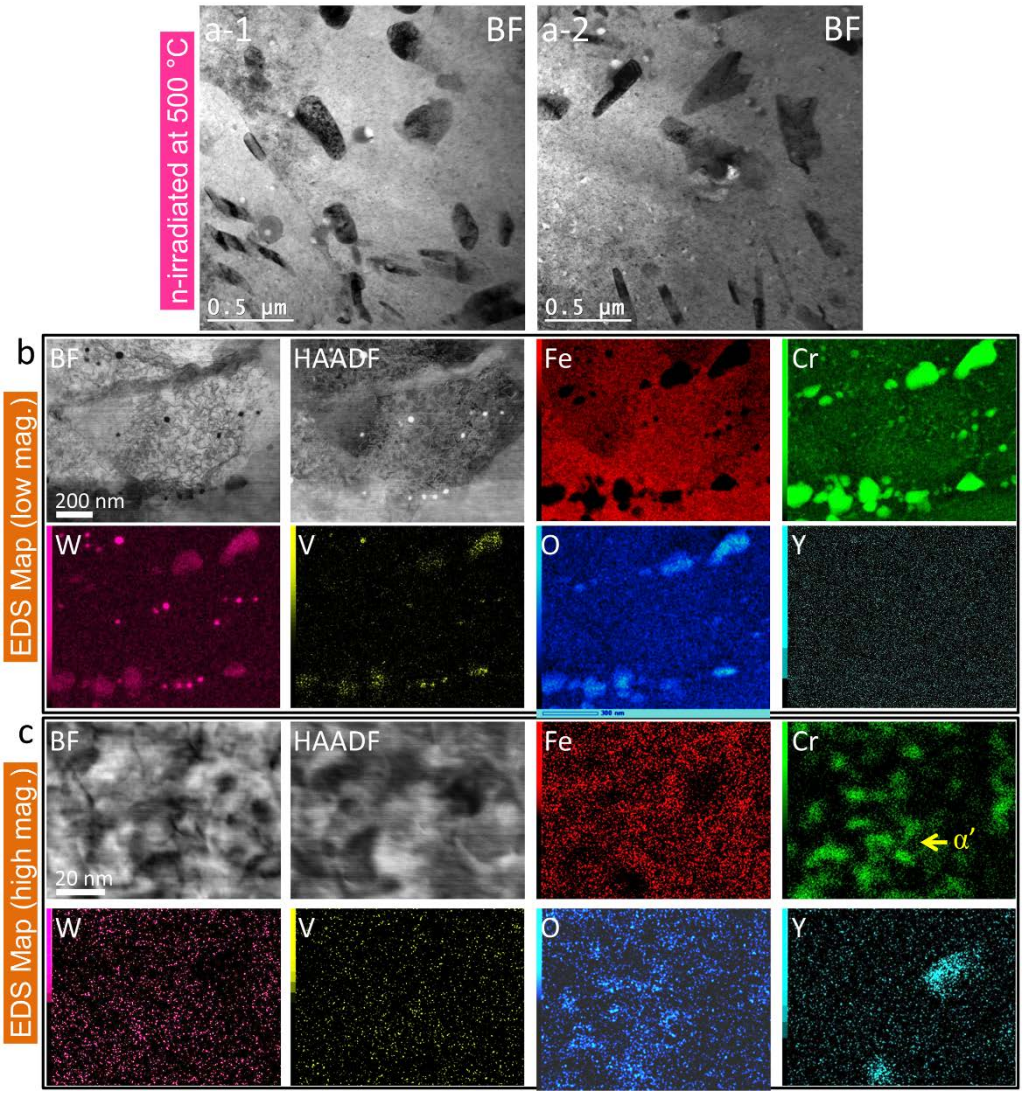

Figure 6. (a) BFTEM images showing particles from the non-injected side of the neutron-irradiated 14YW. BF and HAADF STEM images at (b) low and (c) high magnification with elemental EDS mapping. These maps reveal the presence of several phases, including significant evidence for α′ formation. See text for explanation.

A comparable set of images and STEM-EDS maps were obtained to investigate the particle types and chemical evolution in the He-injected side of 14YW. The results, presented in Figure 7, revealed no major differences compared to the side with no He injection. Small W-V carbides could be found at random in a very low density, while the larger Cr-rich particles are commonly present at lath boundaries. The small Y-rich oxide particles are dispersed more evenly and densely than the other particle types. Interestingly as can be seen in Figure 8, the W-V carbide particles contain a reasonable degree of Cr and V, whereas Cr-rich particles have very low W and V. The W-V carbide particles often exhibit a core-shell structure consisting of a Cr-rich outer shell surrounding a W and V-rich core, raising the possibility that Cr diffuses to the particle interface along with the He and vacancies. This was also found to occur in the F82H.mod3 alloy.

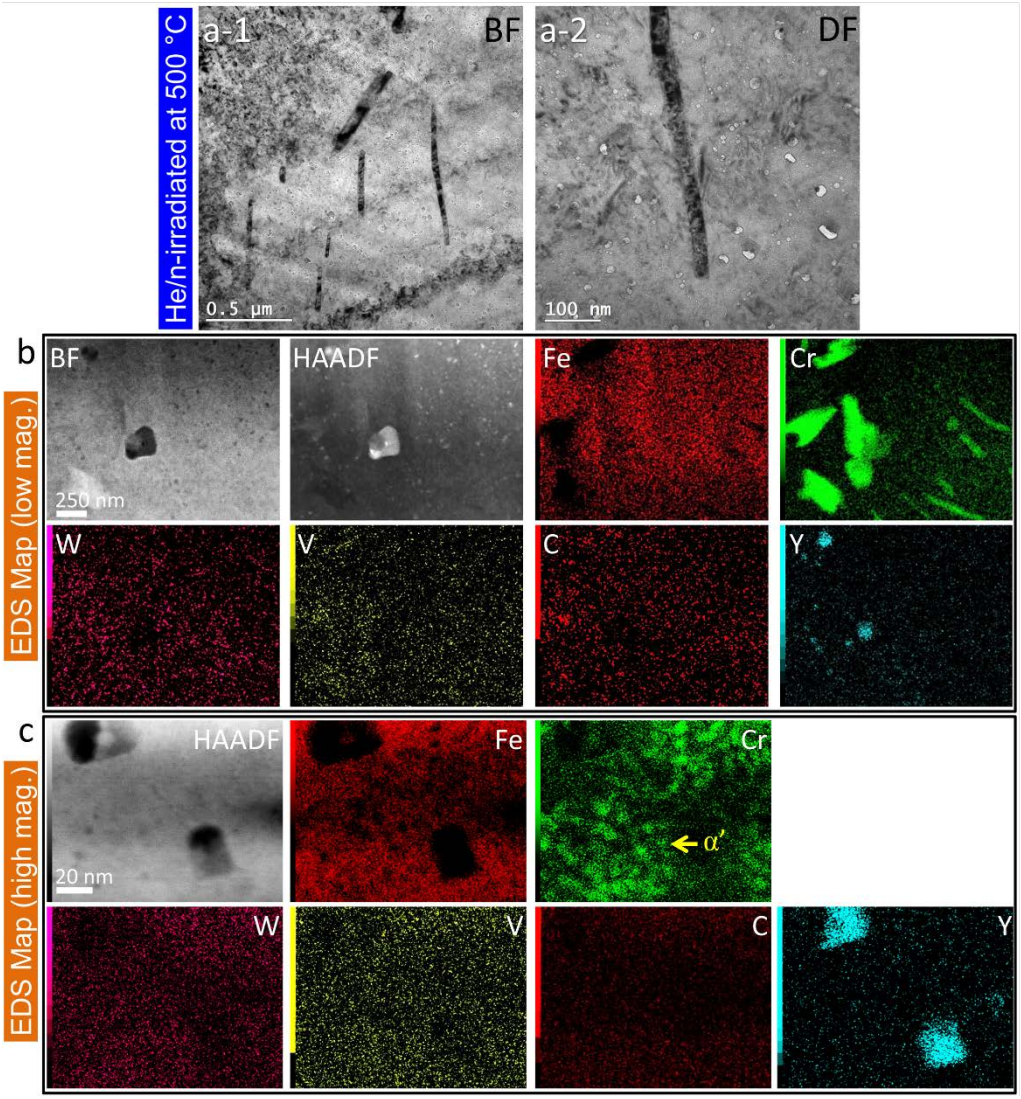

Figure 7. (a) BFTEM images showing particles from He/neutron-irradiated 14YW. BF and HAADF STEM images at (b) low and (c) high magnification with elemental EDS mapping of Fe (red), Cr (green), W (purple), V (yellow) and O (blue), and Y (light blue). There are three types of particles present based on these maps, and Cr-rich α' (Cr map at c) and Y-O matches (Y and O map at c) at high magnification are verified. See text for explanation.

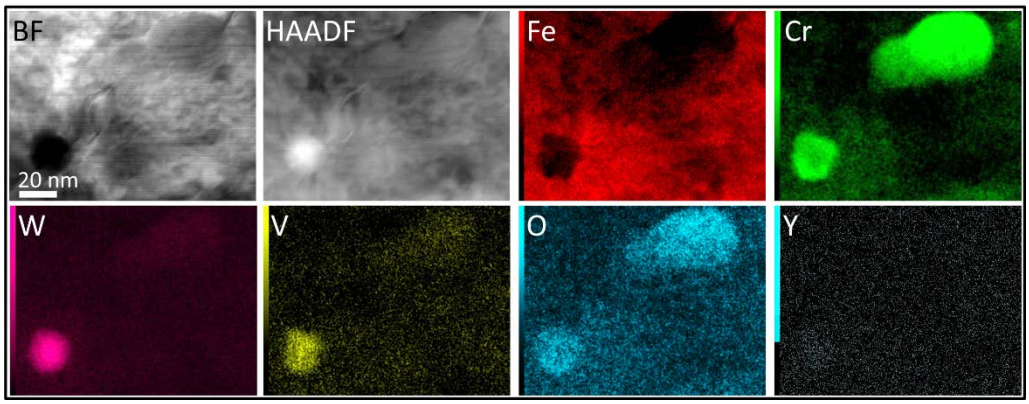

Figure 8. BF and HAADF STEM images with elemental maps taken from the He injected side of the neutron-irradiated 14YW reveal two types of particles: an elongated Cr-rich carbide phase with low concentration of W and V (top right) and a spherical W-rich oxide particle with a moderate concentration of Cr and V (bottom left). Note that W and V are concentrated at core of the W-rich particle, but Cr is concentrated in a shell around the core of the particle.

Figures 9 and 10 reveal line dislocations and dislocation loops of F82H-mod.3+CW and 14YW respectively on two sets of BFTEM images at under/in/over-focus from both sides of the TEM discs. The through-focal series is used to highlight the distribution of cavities with respect to the dislocation structure. Measured densities of line dislocations at each case are given in Table 4, and show that the densities of line dislocations are not significantly different for the two alloys, ranging from 1 to 3×10^{-14} m^{-2}. The BFTEM images indicate that the He-injected side has a higher density of loops than in the non-injected side, and this is currently being investigated in more detail. In our previous report, measured densities of dislocation loops of two samples (regardless of loop types) on the He-implanted side are similar with a range of $3\sim5\times10^{21}$ m^{-3} [11], but the non-injected side had not yet been characterized.

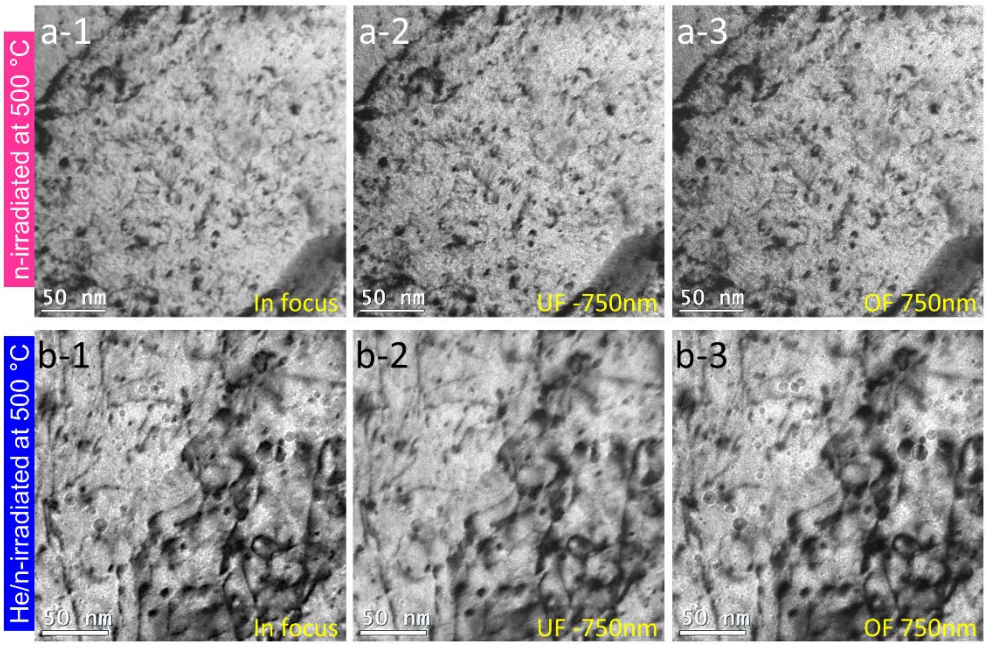

Figure 9. The dislocation structure is shown in two sets of BFTEM images of F82H-mod.3+CW taken at under/in/over-focus from (a) the non-He injected side and (b) the He-injected side

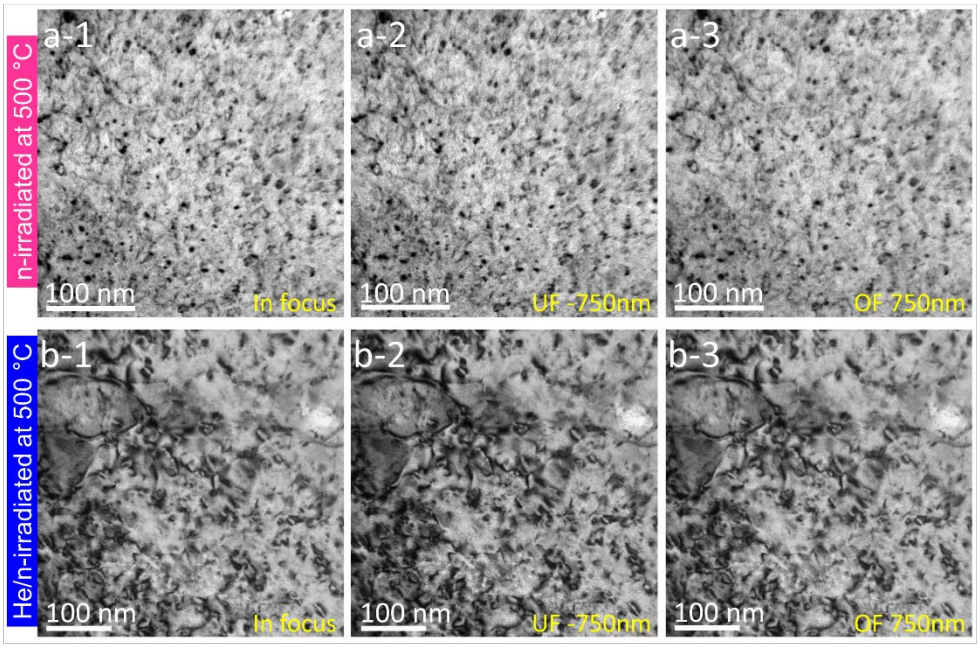

Figure 10. The dislocation structure is show in two sets of BFTEM images taken of the neutron-irradiated 14YW alloy at under/in/over-focus from (a) the non-He injected side and (b) the He-injected side.

Table 4. Density (m^{-2}) of line dislocations in two alloys

Alloy	He-Implanted Side	Non-implanted Side
F82H-mod	2.7×10^{14}	3.0×10^{14}
14YW	2.4×10^{14}	1.6×10^{14}

Acknowledgments

This research was supported by the U. S. Department of Energy, Office of Fusion Energy Sciences, under contract DE-AC06-76RLO1830.

REFERENCES

[1] G. R. Odette, M. J. Alinger, and B. D. Wirth, Annu. Rev. Mater. Res. 38 (2008) 471.
[2] R. J. Kurtz, A. Alamo, E. Lucon, Q. Huang, S. Jitsukawa, A. Kimura, R. L. Klueh, G. R. Odette, C. Petersen, M. A. Sokolov, P. Spätig, and J. W. Rensman, J. Nucl. Mater. 386-388 (2009) 411.
[3] N. Baluc, K. Abe, J. L. Boutard, V. M. Chernov, E. Diegele, S. Jitsukawa, A. Kimura, R. L. Klueh, A. Kohyama, R. J. Kurtz, R. Lässer, H. Matsui, A. MÖslang, T. Muroga, G. R. Odette, M. Q. Tran, B. van der Schaaf, Y. Wu, J. Yu, and S. J. Zinkle, Nucl. Fusion 47 (2007) S696.
[4] H. Ullmaier, Nucl. Fusion. 24 (1984) 1039
[5] R. E. Stoller and G. R. Odette, J. Nucl. Mater. 131 (1985) 118.
[6] R. Schäeublin and Y. L. Chiu, J. Nucl. Mater. 362 (2007) 152
[7] G. R. Odette, P. Miao, D. J. Edwards, T. Yamamoto, R. J. Kurtz, and H. Tanigawa, J. Nucl. Mater. 417 (2011) 1001.
[8] B. Yao, D. J. Edwards, R. J. Kurtz, G. R. Odette, and T. Yamamoto, Fusion Materials Semiannual Progress Report for Period Ending December 31, 2011, DOE/ER-0313/51, U.S. Department of Energy, 85.
[9] B. Yao, D. J. Edwards, and R. J. Kurtz, G. R. Odette, and T. Yamamoto, Maps of dislocation loops in irradiated bcc Fe–based steels. To be submitted.

[10] L. R. Greenwood, B. M. Oliver, S. Ohnuki, K. Shiba, Y. Kohno, A. Kohyama, J. P. Robertson, J. W. Meadows, and D. S. Gelles, J. Nucl. Mater. 283-287 (2000) 1438.
[11] L. R. Greenwood and F. A. Garner, J. Nucl. Mater. 212-215 (1994) 635.
[12] T. Noda, M. Fujita, and M. Okada, J. Nucl. Mater. 258-263 (1998) 934.
[13] T. Tanno, A. Hasegawa, J-C He, M. Fujiwara, S. Nogami, M. Satou, T. Shisido, and K. Abe, Mater. Trans. 48, (2007) 2399.
[14] B. Yao, D. J. Edwards, R. J. Kurtz, G. R. Odette, and T. Yamamoto, Fusion Materials Semiannual Progress Report for Period Ending December 31, 2012, DOE/ER-0313/44, U.S. Department of Energy, 26.
[15] T. Yamamoto, G. R. Odette, P. Miao, D. J. Edwards, and R. J. Kurtz, Fusion Materials Semiannual Progress Report for Period Ending December 31, 2008, DOE/ER-0313/44, U.S. Department of Energy, 44.